Numerical investigation of abradable coating removal in aircraft engines through plastic constitutive law

Mathias Legrand, Alain Batailly, Christophe Pierre

Numerical investigation of abradable coating removal in aircraft engines through plastic constitutive law

Mathias Legrand
mathias.legrand@mcgill.ca, 514-398-5321
Structural Dynamics and Vibration Laboratory, Department of Mechanical Engineering, McGill University, 817 Sherbrooke St West, Montréal, Québec H3A 2K6, Canada

Alain Batailly
alain.batailly@mcgill.ca, 514-398-5321
Structural Dynamics and Vibration Laboratory, Department of Mechanical Engineering, McGill University, 817 Sherbrooke St West, Montréal, Québec H3A 2K6, Canada

Christophe Pierre
christophe.pierre@mcgill.ca, 514-398-5321
Structural Dynamics and Vibration Laboratory, Department of Mechanical Engineering, McGill University, 817 Sherbrooke St West, Montréal, Québec H3A 2K6, Canada

Abstract

In the field of turbomachines, better engine performances are achieved by reducing possible parasitic leakage flows through the closure of the clearance distance between blade tips and surrounding stationary casings and direct structural contact is now considered as part of aircraft engines normal life. In order to avoid catastrophic scenarios due to direct tip incursions into a bare metal housing, implementation of abradable coatings has been widely recognized as a robust solution offering several advantages: reducing potential non-repairable damage to the incurring blade as well as adjusting operating clearances, in-situ, to accept physical contact events. Nevertheless, the knowledge on the process of material removal affecting abradable coatings is very limited and it seems urgent to develop dedicated predicting numerical tools.

The present work introduces a macroscopic model of the material removal through a piecewise linear plastic constitutive law which allows for real time access to the current abradable liner profile within a time-stepping approach of the explicit family. In order to reduce computational loads, the original finite element formulation of the blade of interest is projected onto a reduced-order basis embedding centrifugal stiffening. First results prove convergence in time and space and show that the frequency content of the blade response is clearly sensitive to the presence of abradable material. The continuous opening of the clearance between the blade tip and the casing due to the material removal yields larger amplitudes of motion and new scenarios of structural divergence far from the usual linear conditions provided by the well-known Campbell diagrams.

Keywords: Turbomachinery; Abradable coatings; Wear; Material removal, Contact dynamics; Explicit time-marching technique

1 Introduction

Facing a constant need for improved performances and lower operating costs, jet engine manufacturers respond with modern technologies such as higher casing conicity

for increased compression rates, higher operating temperatures, more efficient aerodynamic designs and lightweight materials, amongst others. One of the technology being addressed involves the reduction of parasitic leakage flows between blade-tips an surrounding casings in compressor and turbine stages (Fig. 1) where minimal operating clearances are required. This is made possible through the implementation of abradable coatings [24] that are deposited onto the casings. The liners are used to maintain

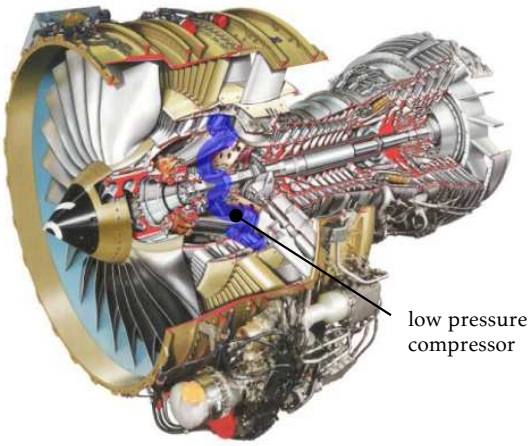

Figure 1: Low pressure compressor. Courtesy of CFM International

tight tolerances between the rotating blades and static fan-case assembly as well as to accept potential physical contact events. The tips abrade the coating so that its shape can conform to the blade trajectory. Such rub events may occur through a variety of mechanisms: coincidence of vibration modes, thermal gradient in the casing, rotor imbalance due to design uncertainties, gyroscopic forces during certain manoeuvres of the aircraft, etc. To accommodate this rubbing, the mechanical properties of the sacrificial abradable material designed to be cut away by the blades are of primary importance. It must be reasonably soft to preserve the incurring blade-tips from damage whilst sufficiently resilient to stand very high temperatures and high-speed gas flows with inherent solid particles [10] and to maintain structural integrity. Destructive side-effects were detected by experimental investigations during which material removal of abradable coatings may have played a significant role in the initiation of divergent structural behaviors such as propagating cracks in blade roots [13]. Coating behaviors akin to *regenerative waviness* found in machining and leading to unbounded blade displacements could also be observed [11, 22]. Accordingly, it seems urgent to enrich the limited current knowledge of the circumstances under which they occur [5].

Attention was brought in the past to the dynamics of blades in the framework of unilateral and frictional contact [18, 9, 8] but modeling the removal process of the abradable coatings in a macroscopic fashion seems rather new. Even though simple analytical derivations [14] as well as more sophisticated numerical investigations [15] do exist, they seem more suited to the slow time-scale kinetics of fretting or erosive wear occurring on limited areas. In the context of turbomachines, where large relative displacements between contacting components together with high abradable wear rates are observed, most of the existing theoretical statements with strongly limiting assumptions do not seem relevant and easy to incorporate, even though some of them look promising [20, 21, 4]. Difficulties stem from high-rate material removal together with complex and coupled physical mechanisms involved such as dislocation, thermal gradients, large displacements [1], and mass ejection.

It is here assumed that plasticity with its inherent abilities to account for permanent deformation in a simple fashion stands as a natural macroscopic approach to describe abradable coating removal during rub with a rotating blade. The mass variation is neglected and the exact dynamics of the abradable material is not retrieved but it is thought that the overall behavior of the blade will be captured and potential critical responses will be properly predicted. Furthermore, the energy transferred from the blade to the casing during contact interaction is partially dissipated because of wear: this can be captured by a plastic constitutive law. Finally, as potentially highly transient, it is proposed to tackle the material removal process and the contact conditions through an explicit time marching technique embedding a contact detection procedure as well as the calculation of internal forces and permanent plastic deformations arising in the abradable material. The introduced approach allows the user-control of the ductility of the abradable liner and the real time access to its current profile, supposedly key feature for detecting such critical behaviors mentioned above.

2 Vocabulary

As already mentioned in the introduction, abradable coatings have been adopted as an industry standard for use in clearance control applications. Attendant rub events affect the abradable layer in ways that could be termed *material removal* or *wear*. These two terms will be used with no distinction in the remainder even though *wear* may be associated with other processes such as *erosion*, *abrasion* or *corrosion* that do not exactly fall in the class of occurrences explored here. In this regard, the abradable coating will be said *ductile* when exhibiting an ability to be easily rubbed away.

The primary objective of this research is to detect potential diverging motions of the blade initiated by abradable removal even though a detailed description of the latter is out of scope.

3 Structural model and equations of motion

3.1 Finite element model

The present study deals with a single rotating blade and a surrounding casing of a low pressure compressor stage, as depicted in Fig. 2. Adjacent blades are assumed to be slightly shorter and their dynamic contribution is ignored. Possible gyroscopic effects or imbalance loads are not accounted for and the supporting shaft is rigid. The infinitesimal kinematic theory framework is used and the reference frame is attached to the rotating blade. The considered sector is discretized in 11,339 prismatic finite elements connected through 22,898 nodes. Within the well-known finite element approach, vector $\mathbf{u}$ stores all the displacement degrees-of-freedom of the blade and the respective mass matrix $\mathbf{M}$, damping matrix $\mathbf{D}$, stiffness matrix $\mathbf{K}$ and contact forces vector $\mathbf{F}^c$ are built accordingly. The resulting governing equation of motion reads:

$$\mathbf{M}\ddot{\mathbf{u}} + \mathbf{D}\dot{\mathbf{u}} + \mathbf{K}(\Omega)\mathbf{u} + \mathbf{F}^c = \mathbf{0} \tag{1}$$

where Ω stands for the rotational frequency and is here included in the stiffness matrix to reflect the linear centrifugal stiffening experienced by the blade of interest: the natural frequencies of vibration are affected but not the geometry. Eq. (1) is complemented with the usual unilateral contact constraints of Signorini type. They control the computation of the coordinates of $\mathbf{F}^c$ and are detailed later in the paper.

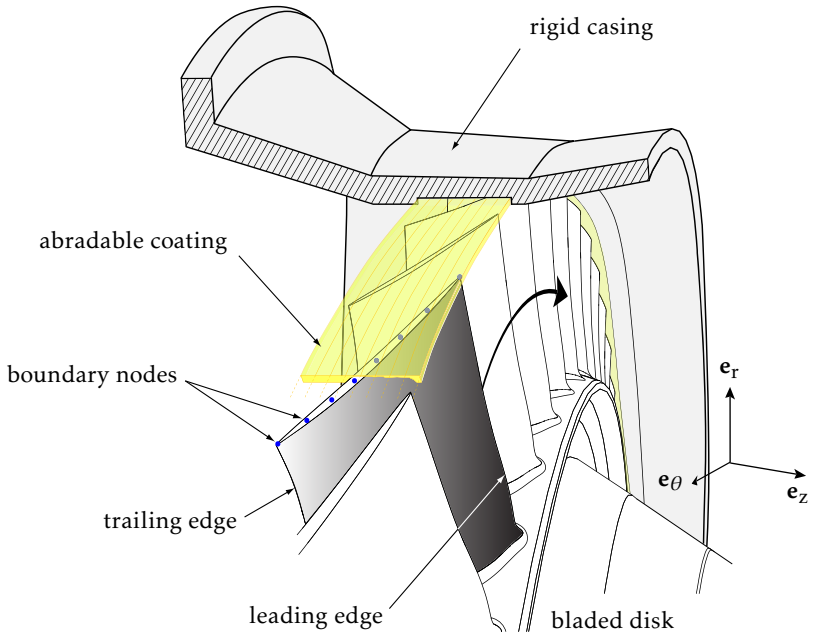

Figure 2: Blade under investigation with eight anticipated boundary nodes undergoing contact constraints and abradable removal conditions

Based on thorough preliminary simulations and experimental data, it is here admitted that the casing remains insensitive to the contact interaction with the blade and is not modeled as a flexible component in the present study.

3.2 Reduced-order model and component mode synthesis

Aircraft engines are characterized by a cold build clearance. In operating conditions, the blade-tips will move outwards under centrifugal loading such that at cruise speeds the system is in an optimum position. The linear contribution of this centrifugal stiffening effect is here embedded in a reduced-order model of the blade since the original finite element formulation (1) is numerically large and leads to unacceptable computation times. The blade is synthesized through a modified version of the Craig-Bampton procedure [3] reported in [19]. The stiffness matrix $\mathbf{K}(\Omega)$ is approximated by a polynomial expansion over a specified rotational frequency range $\Omega \in [0;\Omega_m]$ such as:

$$\mathbf{K}(\Omega) = \mathbf{K}^0 + \Omega^2\mathbf{K}^1 + \Omega^4\mathbf{K}^2 \tag{2}$$

where:

$$\begin{aligned}
\mathbf{K}^0 &= \mathbf{K}(0) \\
\mathbf{K}^1 &= \frac{1}{3\Omega_m^2}\left[16\mathbf{K}\left(\frac{\Omega_m}{2}\right) - \mathbf{K}(\Omega_m) - 15\mathbf{K}(0)\right] \\
\mathbf{K}^2 &= \frac{3}{4\Omega_m^4}\left[\mathbf{K}(\Omega_m) - 4\mathbf{K}\left(\frac{\Omega_m}{2}\right) + 3\mathbf{K}(0)\right]
\end{aligned} \tag{3}$$

The Craig-Bampton transformation matrix mapping the reduced-order space to the original physical one, usually calculated at rest, is here expanded according to Eq. (2). Computation of the reduced-order model is then carried out using three modal reduction bases calculated for $\Omega = 0$, $\Omega = \Omega_m/2$ and $\Omega = \Omega_m$, respectively, which yields the

following transformation matrix $\mathbf{\Phi}$:

$$\mathbf{\Phi} = \begin{bmatrix} \mathbf{I} & \mathbf{0} & \mathbf{0} & \mathbf{0} & \mathbf{0} & \mathbf{0} \\ \mathbf{\Phi}_{\mathrm{R}}(0) & \mathbf{\Phi}_{\mathrm{R}}\left(\frac{\Omega_{\mathrm{m}}}{2}\right)^{*} & \mathbf{\Phi}_{\mathrm{R}}(\Omega_{\mathrm{m}})^{*} & \mathbf{\Phi}_{\mathrm{L}}(0) & \mathbf{\Phi}_{\mathrm{L}}\left(\frac{\Omega_{\mathrm{m}}}{2}\right) & \mathbf{\Phi}_{\mathrm{L}}(\Omega_{\mathrm{m}}) \end{bmatrix} \tag{4}$$

where matrices $\mathbf{\Phi}_{\mathrm{R}}(\Omega)$ and $\mathbf{\Phi}_{\mathrm{L}}(\Omega)$ stand for the n_{c} constraint modes and the η fixed-interface modes computed at Ω, respectively. Superscript * indicates that matrix $\mathbf{\Phi}_{\mathrm{R}}(0)$ is subtracted: $\mathbf{A}^{*} = \mathbf{A} - \mathbf{\Phi}_{\mathrm{R}}(0)$. Matrix $\mathbf{\Phi}$ in Eq. (4) defines the projection used to reduce the size of the investigated system. It is potentially rank-deficient because of similarities between the calculated constraint modes. An orthonormalization which relies on a singular value decomposition is thus performed. It yields a reduction of the rank and the maximum dimension of the subsequent reduced-order model is $n = 3\eta + 3n_{\mathrm{c}}$.

Accordingly, the original equations of motion (1) are projected onto the newly built reduced-order space as follows:

$$\mathbf{u} = \begin{pmatrix} \mathbf{u}_b \\ \mathbf{u}_i \end{pmatrix} = \begin{bmatrix} \mathbf{I} & \mathbf{0} \\ \mathbf{\Phi}_R(0) & \mathbf{\Psi} \end{bmatrix} \begin{pmatrix} \mathbf{u}_b \\ \mathbf{q} \end{pmatrix} \tag{5}$$

where the reduced displacement vector $(\mathbf{u}_b\ \mathbf{q})^{\mathrm{T}}$ is substantially smaller than the original physical displacement vector $(\mathbf{u}_b\ \mathbf{u}_i)^{\mathrm{T}}$. The dynamics of the considered blade is now seen as a full set of constraint modes whose contributions $\mathbf{u}_b$ are the physical displacements of the interface dof, complemented with a set of component modes of contribution $\mathbf{q}$ that control the precision of the numerical simulations. As deduced from Eq. (5), the contact constraints can directly be treated in the reduced space if the anticipated contact locations are defined as interface nodes, thus avoiding permanent forward and backward mappings to the physical space. This is a major feature motivating the choice of the Craig-Bampton technique.

In this study, eight nodes, numbered from the leading edge to the trailing edge as illustrated in Fig. 2, define the discretized contact interface. To ensure linear modal convergence, at least six component modes are required for each of the three considered rotational frequencies Ω and the final size reduced-order model of the blade is 85 DoF. It is considered that linear modal convergence is reached when the difference between the first N eigenfrequencies of the finite element model and the corresponding eigenfrequencies of the reduced-order model is less than 1%.

The performances of the computed reduced-order model are characterized by comparing the resulting Campbell diagram to the Campbell diagram of the associated full finite element model, as displayed in Fig. 3 where frequencies are normalized with respect to the first natural frequency of the structure at rest. It is shown that the built reduced-order model accurately predicts the first seven frequencies over the selected rotational frequency range.

An evident shortcoming of the reduced-order model is that the selected interface nodes do not include any information on the *exact* geometry of the blade-tip. For abradable profile convergence purposes, this geometry is numerically incorporated back into the solution strategy, as illustrated in Fig. 4. It is also now understood that Eq. (1) has undergone projection (5) so that the dimension of the system is already reduced even though notations are not adjusted for readability.

4 Contact dynamics

In order to compute the contact force vector $\mathbf{F}^{\mathrm{c}}$ in Eq. (1), derivation of the governing equations is conducted in the context of contact mechanics [6, 23]. By choice, the blade

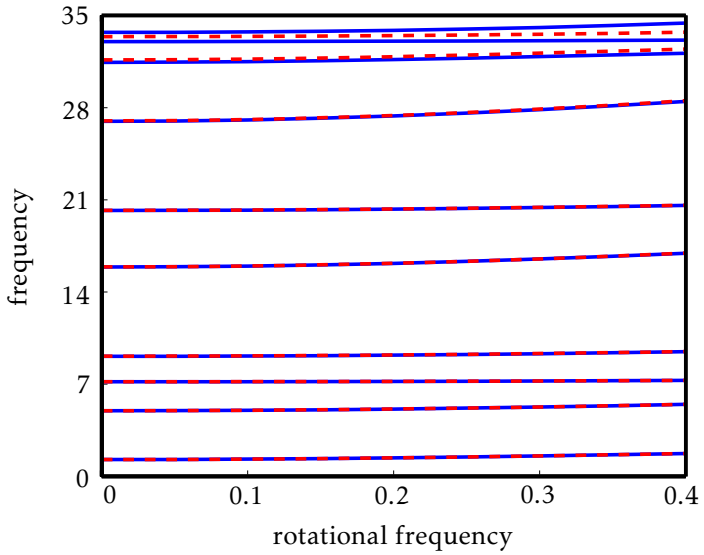

Figure 3: Campbell diagrams with centrifugal stiffening: reduced-order model (– –) and full finite element model with no parametrization of the stiffness matrix (——)

supports the master surface Γ_c^m from which the abradable coating can be parameterized. It is then possible to find for any material point $\mathbf{x} \in \Gamma_c^m$, restricted here to the interface nodes previously defined, its closest counterpart $\bar{\mathbf{y}}$ on the abradable material slave surface Γ_c^s:

$$\bar{\mathbf{y}} = \arg\min_{\mathbf{y}\in\Gamma_c^s} \|\mathbf{x}-\mathbf{y}\| \tag{6}$$

According to these notations, the discretized clearance between the two components can be stated as:

$$\mathbf{g}(\mathbf{x}) = \mathbf{g}_0(\mathbf{x}) + \left(\mathbf{u}^m(\mathbf{x}) - \mathbf{u}^s(\bar{\mathbf{y}}(\mathbf{x}))\right)\cdot\mathbf{n} \tag{7}$$

where $\mathbf{g}_0(\mathbf{x})$ represents the initial positive gap and $\mathbf{n}$, the outward normal to Γ_c^s. The contact conditions, referred to as the Kuhn-Tucker optimality conditions, considered in a vector-compact form[1], are such that:

$$\forall \mathbf{x} \in \Gamma_c^m, \qquad \mathbf{t}_N \geq 0, \quad \mathbf{g}(\mathbf{x}) \geq 0, \quad \mathbf{t}_N\,\mathbf{g}(\mathbf{x}) = 0 \tag{8}$$

where $\mathbf{t}_N$ stands for the discretized contact pressure, assumed positive when acting on the contact interface. The initial clearances go from $1.5\cdot10^{-2}\%$ to $4.3\cdot10^{-2}\%$ of the blade length from the leading to the trailing edges.

In this study, the contact pressure $\mathbf{t}_N$ as well as the operating clearance $\mathbf{g}(\mathbf{x})$ in Eq. (8) are implicitly and inherently related to the abradable modeling which is discussed next.

5 Abradable constitutive law with plasticity

One of the challenges associated with the numerical prediction of the mechanical behavior of abradable materials is the fact that the coating features that promote rub-tolerance, such as friability, low shear strength, thermal and melting properties can result in very complicated mechanisms that are extremely difficult to tackle. The present

[1] These conditions written in a vector form have to be read coordinate by coordinate for each interface dof where contact is treated.

study pretends that the potentially incurring blade machines its way into the stator during a run-in procedure or in engine operating conditions by squashing the facing layer of abradable which undergoes plasticity. In this macroscopic strategy, the abradable coating is discretized with one-dimensional two-node rod elements as detailed in Fig. 4. Each element is independent from its adjacent neighbors. Over the thickness

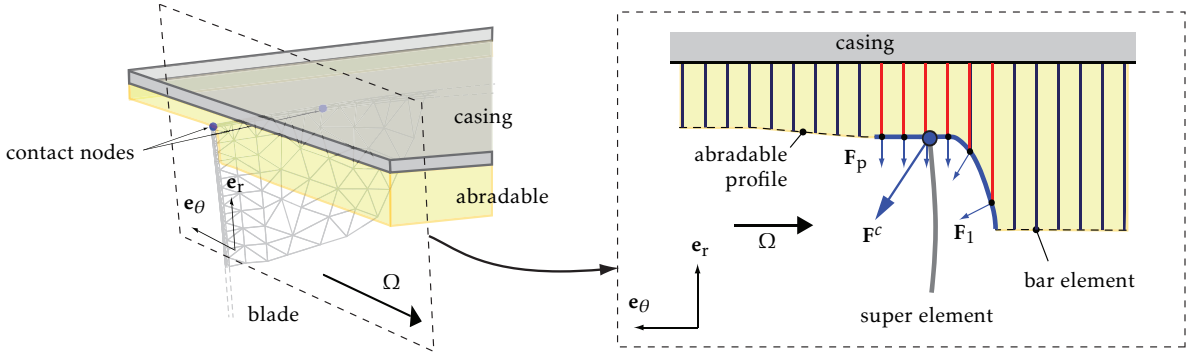

Figure 4: Blade interface node and associated geometrical profile

of the abradable layer, a single element is used since calculations are performed in a quasi-static compression framework only. The *density* ν of the abradable coating, *i.e.* the number of elements situated along the circumference of the case housing, is left to investigation.

By convention, strains ε and stresses σ are such that $(\varepsilon, \sigma) \in \mathbb{R}^+ \times \mathbb{R}^+$. The set of admissible stresses $\mathbb{E}_\sigma$ is defined as [17]:

$$\mathbb{E}_\sigma = \{(\sigma, \alpha) \in (\mathbb{R}, \mathbb{R}) \,|\, f(\sigma, \alpha) \leq 0\} \tag{9}$$

where $\alpha : [0, T] \rightarrow \mathbb{R}$ is an internal hardening variable and f, a yield function. It is also assumed that (1) the total strain is separated in an additive way between its elastic part ε^e and plastic part ε^p such as $\varepsilon = \varepsilon^e + \varepsilon^p$ and (2) the relation between elastic strains and stresses is linear $\sigma = E\varepsilon^e$. By choice hardening is isotropic. It corresponds to a uniform expansion of the initial yield surface with no translation. In other words, the origin of $\mathbb{E}_\sigma$ does not move and the hardening is linear along the plastic flow which dictates the evolution of the plastic strain $\Delta\varepsilon^p$. This leads to the definition of f:

$$f(\sigma, \alpha) = \sigma - (\sigma_Y + K\alpha) \tag{10}$$

where $\sigma_Y > 0$ stands for the elastic limit and $K \geq 0$, for the plastic modulus of the abradable material, quantities illustrated in Fig. 5 along with the Young modulus E. The second assumption yields:

$$\Delta\alpha = \Delta\varepsilon^p \tag{11}$$

and the condition on the plastic flow implies the existence of a consistency parameter γ, such as $\Delta\varepsilon^p = \gamma \frac{\partial f}{\partial \sigma}$, equivalent to $\Delta\varepsilon^p = \gamma$ because of Eq. (10). Dual variables γ and f obey the Kuhn-Tucker conditions, complemented by the consistency condition:

$$\gamma \geq 0, \quad f(\sigma, \alpha) \leq 0, \quad \gamma f(\sigma, \alpha) = 0, \quad \gamma \Delta f(\sigma, \alpha) = 0 \tag{12}$$

In a one-dimensional quasi-static strain formulation, the solution strategy is greatly simplified even though the nonlinear nature of the constitutive law can be accounted for

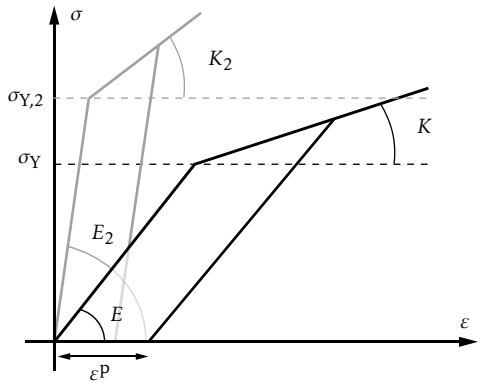

Figure 5: Plasticity constitutive laws controlling the ductility of the abradable coating

by incremental techniques only. Consider an admissible state together with a prescribed increment of deformation $\Delta\varepsilon$ within a purely elastic trial state:

$$\begin{aligned} &\sigma^{\text{trial}} = E\Delta\varepsilon + \sigma \\ &\Delta\varepsilon^p = 0 \\ &\Delta\alpha = 0 \\ &f^{\text{trial}} = \sigma^{\text{trial}} - (\sigma_Y + K\alpha) \end{aligned} \tag{13}$$

In order to ensure that the trial state belongs to $\mathbb{E}_\sigma$, f^{trial} is tested:

- if $f^{\text{trial}} \leq 0$, trial and current states coincide;
- if $f^{\text{trial}} > 0$, condition $(12)_2$ is violated and the trial state has to be corrected. The commonly adopted approach, namely the *Return Mapping Algorithm* [16], lies in the projection of the trial state on the boundary of the yield function $f = 0$ together with $\gamma > 0$ at constant strain. Variation of Eq. (10) yields:

$$f = f^{\text{trial}} - \gamma\,(E + K) \tag{14}$$

Consequently, $f = 0$ implies:

$$\gamma = \frac{f^{\text{trial}}}{E + K} \tag{15}$$

and the following update is used:

$$\begin{aligned} &\sigma = \sigma^{\text{trial}} - E\gamma \\ &\Delta\varepsilon^p = \gamma \\ &\Delta\alpha = \gamma \end{aligned} \tag{16}$$

The internal forces acting within each abradable element i are computed in accordance with the above mentioned procedure. During a contact phase, the virtual work of the internal forces acting within the abradable coating for a radial virtual displacement $\boldsymbol{\delta}\mathbf{u}_r$ of the blade is equal, by definition, to the virtual work of the contact force for the same virtual displacement. By defining $I = \{i\,|\,\mathbf{g}(i) = 0\}$ (red bar elements in Fig. 4), equilibrium of the contact forces $\mathbf{t}_N$ in Eq. (8) with the internal forces can be written as:

$$\mathbf{t}_N = \sum_{i \in I} A_i \sigma_i \tag{17}$$

where A_i stands for the cross-section area of an abradable element and depends on the density parameter ν. Also, in order to approximately reflect tangential efforts acting on the blade, the computed contact force on each abradable element is assumed to be *normal to the numerical profile* as displayed in Fig. 4, thus providing both tangential and normal components to the resulting contact force $\mathbf{F}^c$. The ratio between these two components is mostly controlled by the chosen blade-tip geometrical profile itself. Also, as a first approximation, it is assumed that blade displacements in the axial direction ($\mathbf{e}_z$ in Fig. 2) can be ignored in the contact and material removal procedure. To summarize, the role of the plastic constitutive law is threefold:

- compute the normal contact forces exerted by the blade onto the respective abradable coating elements and vice-versa.
- reflect a global tangential effort acting on the blade *only*.
- store the current abradable coating profile through permanent plastic deformations.

6 Time-marching procedure

6.1 Background

The phenomenon under investigation is inherently highly dynamically transient and making use of time stepping techniques, either implicit or explicit, seems quite natural. No matter how, solving the coupled nonlinear governing Eqs. (1) and (17) is a difficult task that requires full attention. As discussed in most of the literature, explicit and implicit approaches offer specific advantages and deficiencies. Among the scientific community has now been reached a consensus stipulating that explicit schemes were simpler and more straightforward to implement and implicit ones were consistently better formulated. It also turns out that depending on the nonlinear terms involved in the governing equations, such as smooth cubic restoring forces versus impact or plastic evolution laws, for instance, classification of the available approaches remains unclear. Nevertheless, explicit techniques do not necessitate the calculation of tangent matrices as required in Newton-like algorithms inherently used in implicit procedures and are thus adopted here. Nevertheless, great care is required in ensuring that the chosen time step does not yield erroneous results as no residual term is checked during algorithmic steps.

By noting $\mathbf{u}_{n+1}$, the numerical approximation of the exact value $\mathbf{u}(t_{n+1})$ at time $t_{n+1} = t_n + h$ where h is the constant time-step, the classical explicit central finite difference scheme used in this work yields:

$$\ddot{\mathbf{u}}_n = \frac{\mathbf{u}_{n+1} - 2\mathbf{u}_n + \mathbf{u}_{n-1}}{h^2} \quad \text{and} \quad \dot{\mathbf{u}}_n = \frac{\mathbf{u}_{n+1} - \mathbf{u}_{n-1}}{2h} \tag{18}$$

6.2 Solution method

The contact detection as well as the internal force contribution of the abradable material are handled by the prediction/correction technique developed in [2] and proved to be relevant in such situations. The final algorithm is then divided into four steps:

1. **prediction**, at time step $n+1$, of the displacements $\mathbf{u}$ of the blade by neglecting the presence of the abradable coating. This predicted displacement, with subscript $_p$,

is expressed as:

$$\mathbf{u}_{n+1,p} = \left[\frac{\mathbf{M}}{h^2} + \frac{\mathbf{D}}{2h}\right]^{-1} \left(\left(\frac{2\mathbf{M}}{h^2} - \mathbf{K}\right)\mathbf{u}_n + \left(\frac{\mathbf{D}}{2h} - \frac{\mathbf{M}}{h^2}\right)\mathbf{u}_{n-1}\right) \tag{19}$$

where displacements $\mathbf{u}_n$ and $\mathbf{u}_{n-1}$ are known.

2. **determination** of the gap function vector $\mathbf{g}_{n+1,p}$ between the two contacting components using Eq. (7). A search algorithm identifies all abradable elements $i \in I$ being penetrated by the blade contact interface.

3. **abradable internal forces computation** through a deformation increment $\Delta\varepsilon$ induced by the predicted penetrations between the two bodies. Subsequent strains $\sigma_{i\in I}$, hardening variables $\alpha_{i\in I}$ and plastic deformations $\varepsilon^p_{i\in I}$ are updated using the above mentioned procedure. The final vector of internal forces is calculated through Eq. (17) and the abradable profile is then updated.

4. **displacements correction** compatible with the calculated contact forces in the normal direction and addition of a global tangential component acting on the blade, both stored in $\mathbf{F}^c$:

$$\mathbf{u}_{n+1} = \mathbf{u}_{n+1,p} - \left[\frac{\mathbf{M}}{h^2} + \frac{\mathbf{D}}{2h}\right]^{-1} \mathbf{F}^c \tag{20}$$

The configuration where the abradable coating is totally removed is not treated in the present work.

6.3 Convergence analysis

The stability and convergence properties of the suggested numerical tool essentially depend on the size of the reduced-order model, the number of interface degrees-of-freedom, the circumferential density of the abradable discretization as well as the time-step size with mutual coupling. Due to the class of nonlinearities and occurrences involved, an analytical derivation of the best compromise of these three parameters to ensure convergence is an illusion. Instead, a semi-empirical numerical drive is carried out. It is understood that the size n of the reduced-order model is adopted in view of Fig. 3 and the number of interface nodes is not discussed.

In order to initiate the contact between the blade and surrounding rigid casing, a temperature gradient equivalent to a multi-harmonic two-nodal diameter external load quasi-statically distorts the casing to absorb the initial clearances, as schematized in Fig. 6(a). The contact and material removal solution method involves eight boundary nodes located on the blade-tip, together with their respective abradable layer, but can be generalized to more nodes at the expense of CPU consumption. The blade meets the casing at least twice per round depending on the calculated amount of material removal. The latter directly depends on the *ductility* which is governed by the plastic law parameters E, K, and σ_Y illustrated in Fig. 5.

Each simulation is conducted on a time interval $t \in [0, T_f]$ where T_f is normalized with respect to twenty rounds of the blade and is thus Ω-dependent. The depicted vibratory and material removal amplitudes are normalized with respect to the initial gap between interface node 1 and the casing.

The convergence in space and time of the wear law is first inspected. This is respectively achieved by increasing the density of abradable elements around the casing

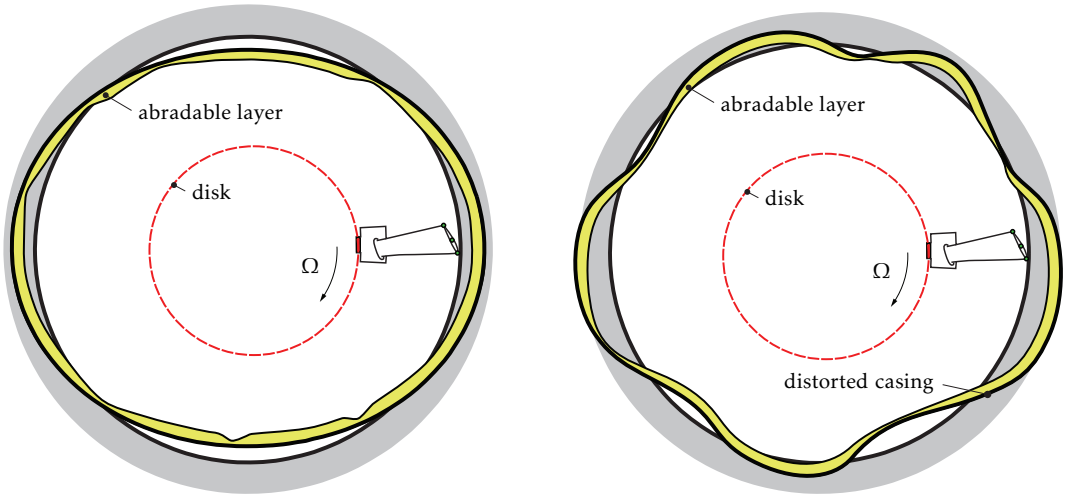

(a) Multi-harmonic 2-nodal diameter distortion (b) Coupled 2- and 5-nodal diameter distortion

Figure 6: Casing distortion in the radial direction

and by reducing the time-step of the time-marching algorithm until convergence is observed. The profile of the abradable coating has to be ν-independent. Figs. 7 depict the final profiles for two densities ν_1 and ν_2 with $\nu_2 \gg \nu_1$, identical time-step and two rotational frequencies. The insignificant differences indicate that convergence with re-

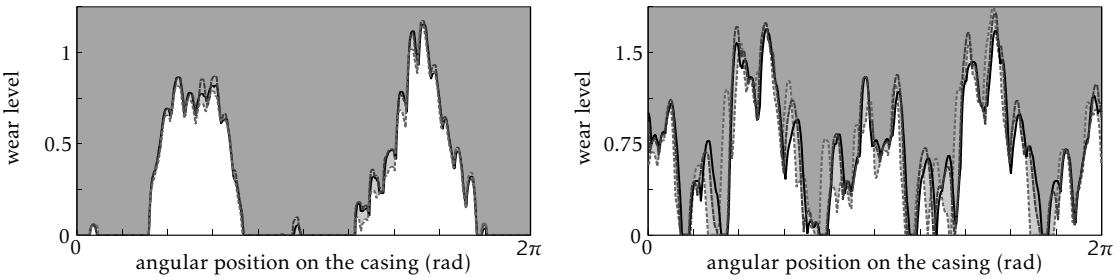

(a) Low rotational frequency (b) High rotational frequency

Figure 7: Final abradable profiles for two densities after twenty rounds of the blade

spect to the density parameter is reached. In other words, there is a density threshold over which the profile becomes invariant for a given configuration. The vibratory behavior of the blade respective to Fig. 7(a) is pictured in Fig. 8(a). The differences are (almost) undistinguishable and therefore, it is assumed that the space-convergence of the material removal macroscopic law is obtained. Convergence in time is displayed in Fig. 8(b) where the displacement of interface node 1 for three different time steps is shown. Similarly, these results ascertain that the time-step for which the algorithm is stable is reached.

It is also worth mentioning that the computation time is not highly dependent on the density parameter ν since it only arises in the correction step of the proposed algorithm. In the sequel, a density parameter offering the best compromise between efficiency and accuracy is chosen.

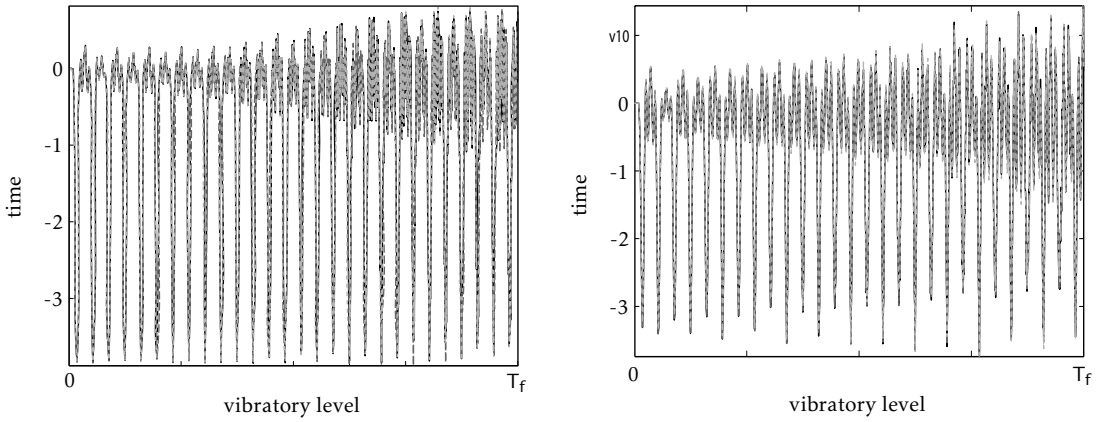

(a) Increasing abradable densities (b) Decreasing time-steps

Figure 8: Radial displacement of interface node 1

7 Main results

In the sequel, the abradable removal process and its possible consequences on the blade vibratory amplitudes are explored and the analysis is mainly performed on the displacement field. However, the proposed strategy easily allows for the computation of strain and stress fields within the blade at any time step of the simulation through transformation (5). It is then possible to identify sensitive areas where stresses may reach critical values and potentially initiate cracks.

Time-marching simulations are carried out for a sequence of rotational frequencies (equivalently termed *rotational velocities*) over $\Omega = [0;\ 0.4]$ with identical initial conditions. Unless explicitly expressed, tangential contact efforts are neglected and the contact configuration is the one depicted in Fig. 6(a). A Fourier transform of the radial displacement of interface node 1 is then performed over the last ten rounds of the blade. These frequency domain results are complemented with maps of material removal and spectrograms. Attention is given to the sensitivity of the sought solution to plastic law parameters E and K while $\sigma_Y = 10^{-8}$ is kept constant.

7.1 Modal analysis and material removal profile

A basic linear modal analysis of the blade is required to bring useful insight to the up-coming results. The first five natural modes of vibration computed at rest are displayed in Fig. 9. Within the operating range of interest, these modes are expected to be excited in a dangerous manner through coupled structural contact and abradable removal mechanisms with a dominant contribution of mode 1 (Fig. 9(a)). Its natural frequency is denoted by $f_1(\Omega)$ where the Ω-dependency emanates from the centrifugal stiffening. Subsequent results expressed in the frequency domain and rotational frequencies are normalized with respect to $f_1(0)$. Simulations were conducted in order to assess the sensitivity of the abradable material removal law and respective worn profiles to the rotational frequency Ω. The n^{th} frequency of the blade will be reached for critical rotational frequencies such as:

$$\Omega = \frac{f_n(\Omega)}{k}, \quad k \in \mathbb{N}^* \tag{21}$$

Condition (21) describes engine-order lines $\text{eo}(k) = k\Omega$ of order k crossing the Ω-dependent and possibly nonlinear frequencies of resonance of the blade. By definition, the order k

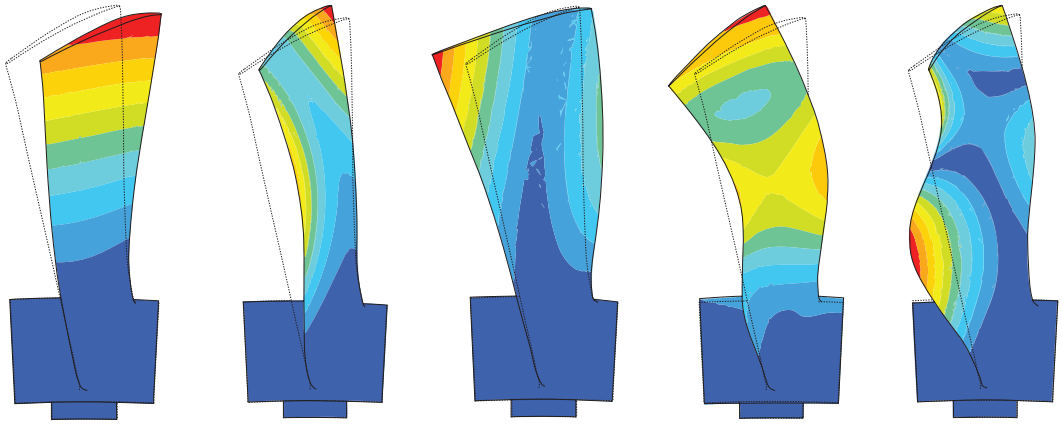

(a) Mode 1 (b) Mode 2 (c) Mode 3 (d) Mode 4 (e) Mode 5

Figure 9: First natural modes of the blade

is any positive integer even though the assumed shape of the casing which implies an engine-order two fundamental component in the response of the blade favors even integers, as displayed in Fig. 10(b) most notably. Due to the presence of superharmonics in the response, condition (21) will thus be satisfied for lower rotational frequencies than a purely linear configuration involving a perfect mono-harmonic two-nodal diameter shape on the casing where $k = 2$ only would be eligible.

Also, it is known that unilateral contact conditions tend to stiffen the flexible mechanical components involved in the contact interaction and modulate their frequency of resonance, phenomenon that is well captured by nonlinear modal analyses [7]. Accordingly, Eq. (21) should be simply revisited as follows:

$$\Omega = \frac{f_n(\Omega, |\mathbf{F}^c|)}{k}, \quad k \in \mathbb{N}^* \tag{22}$$

where $|\mathbf{F}^c|$ refers to the amplitude of the contact forces. At this stage, it is important to keep in mind that the contact forces directly depend on the mechanical properties of the abradable liner, and more specifically on parameter E.

The Ω-dependency of the natural frequencies of the blade is well captured by the reduced-order model since the peaks of resonance are located in a very close neighborhood of the theoretical value which is highlighted by the red curve in the $(f\,;\,\Omega)$ plane. As shown in Figs. 10(a) and 10(b), the spectrum of the blade response is affected by parameter E as follows:

- the *amplitude* of the peak of resonance is significantly larger for a less-ductile abradable.
- the *rotational frequency* for which the peak of resonance occurs is slightly higher for a less-ductile abradable.

Supplementing maps of material removal provided in Figs. 11(a) and 11(b) show the amount of wear and the associated number of worn lobes for each Ω. For low or high rotational frequencies, the shape of the casing controls the worn profile since the blade does not respond in resonance to the nonlinear contact and wear conditions: accordingly, only two lobes are rubbed-away. On the contrary, when Eq. (22) is (nearly) satisfied, large amplitudes of vibration are expected: this is clear for even harmonics $k = 4$

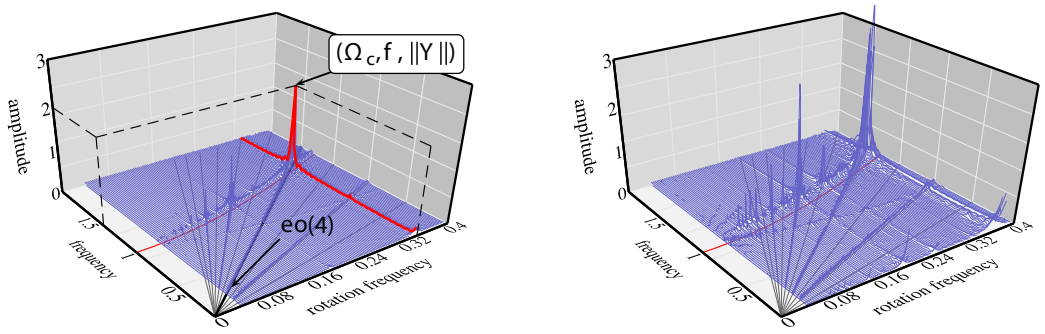

(a) for high ductility $E = 1$ and $K = 0.45$ (b) for low ductility $E = 10$ and $K = 0.45$

Figure 10: Blade response spectrum

and $k = 6$ where four lobes and six lobes are distinguishable, respectively. Superharmonics $k = 8, 10, 12, 14$ are also apparent in Fig. 11(b) at lower rotational frequencies. These maps of worn patterns are also important because they reveal the contact locations between the blade and the casing. Nonlinear resonance conditions are self-organized in such a way that the contact locations are time-independent. Intuitively, one can state that moving contact locations would evenly remove the abradable liner eventually destroying the conditions of resonance leading to a paradox. At the same time, the detection of yet a slight resonance for $k = 5$ is unclear since the symmetry of the casing shape cannot be well described by the corresponding pattern with stationary rub locations.

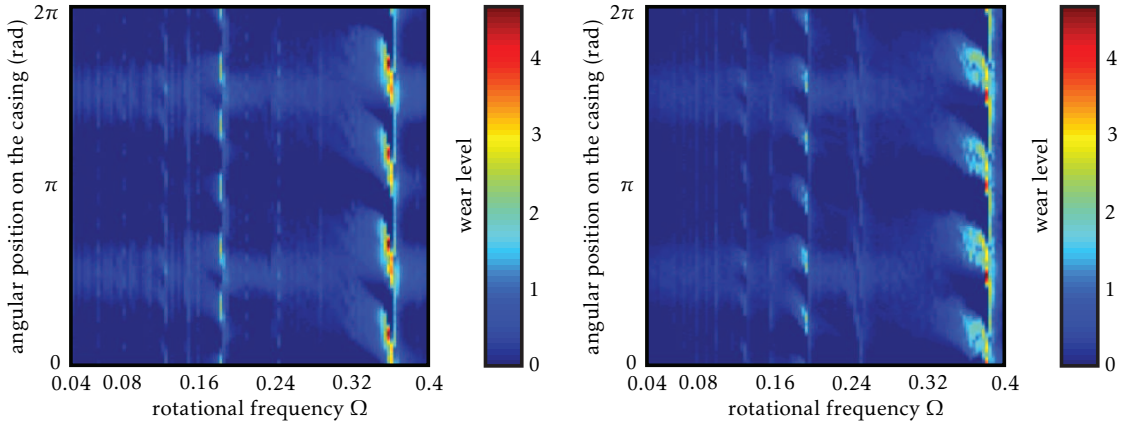

(a) with high ductility $E = 1$ (b) with low ductility $E = 10$

Figure 11: Maps of the final abradable profiles with respect to Ω for interface node 1 after twenty rounds of the blade

Also, from Eq. (21), high amplitudes of vibration should be observed at $\Omega = 0.31$ ($k = 4$) and 0.17 ($k = 6$), velocities located at the intersection of $f_1(\Omega)$ and eo(k). Nevertheless, both peaks of resonance are observed for slightly higher rotational velocities: $\Omega = 0.35$ ($k = 4$) and $\Omega = 0.18$ ($k = 6$) for $E = 1$ and $\Omega = 0.38$ ($k = 4$) and $\Omega = 0.2$ ($k = 6$) for $E = 10$, in perfect concordance with Figs. 10(a) and 10(b). The contact stiffening effect of Eq. (22) is well captured and gives credit to the proposed algorithm.

Also, Figs. 10(b) and11(b) show a minor resonance of the blade along eo(5) with respective worn lobes at $\Omega = 0.24$. This is not unexpected in this highly nonlinear context but it illustrates the relevance of condition (22) although even engine-orders

seem more threatening.

Final abradable patterns for $k = 4$ observed in Figs. 11(a) and 11(b) for $\Omega = 0.35$ and $\Omega = 0.38$, respectively, are compared in Fig. 12. The expected four lobes are obvious as are the differences along the amount of material removal. Results are potentially counter-intuitive since higher wear is observed for less ductile coatings. This is analyzed in the next section.

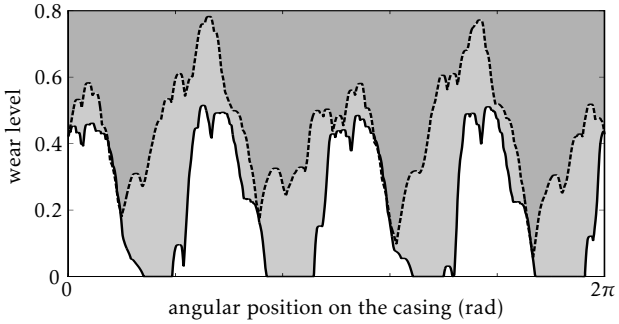

Figure 12: Final abradable profiles for $E = 1$ (——) and $E = 10$ (– –) at respective critical rotational frequency for $k = 4$ after twenty rounds

7.2 Sensitivity analysis

7.2.1 Abradable coating mechanical properties

As explained in the preceding sections, the blade may experience large modal contributions at critical rotational velocities due to intermittent contact and concurrent abradable wear phenomena on the surrounding casing. Nevertheless, it seems quite arduous to recognize a tangible correlation between the abradable mechanical properties and the eventuality of unsuspected large vibratory blade displacements. As a consequence, the maximum amplitude $\|Y\|$ of the main peak of resonance and the *critical* rotational frequency Ω_c for which it emerges, both highlighted in Fig. 10(a), are now examined with respect to parameters E and K over a range reported in Tab. 1.

Young modulus E	1; 1.82; 4.55; 10; 13.64; 18.18; 45.55; 100; 181.82
Plastic modulus K	0.45; 0.91; 4.55; 9.09; 45.45

Table 1: Investigated material properties

Quantities $\|Y\|$ and Ω_c are plotted as histograms. Figure 13(a) attests a bell-shaped evolution of $\|Y\|$ with the existence of a worst-case scenario for $(E;K) = (10;4.55)$. This suggests that when the Young and plastic modulii are small, the abradable is too ductile to support consequent contact forces. The blade erodes the abradable liner without facing resistance and no dangerous interaction may be observed. When both Young and plastic modulii reach extreme values, the configuration is very similar to direct unilateral contact between the blade-tip and the rigid casing and the displacements are limited to the existing initial separating clearance. For intermediate values, the coating will be slowly worn away so that the blade is exposed to an operating clearance which continuously grows with time and the number of revolutions covered by the blade, and is simultaneously fed with energy stemming from the rotation of the engine and intermittent contact. This self-sustained harmful combination similar to regenerative waviness in machining sketches an interaction scenario slowly but resolutely leading

to unbounded blade displacements (see Fig. 8). Figure 13(b) underlines the role of the

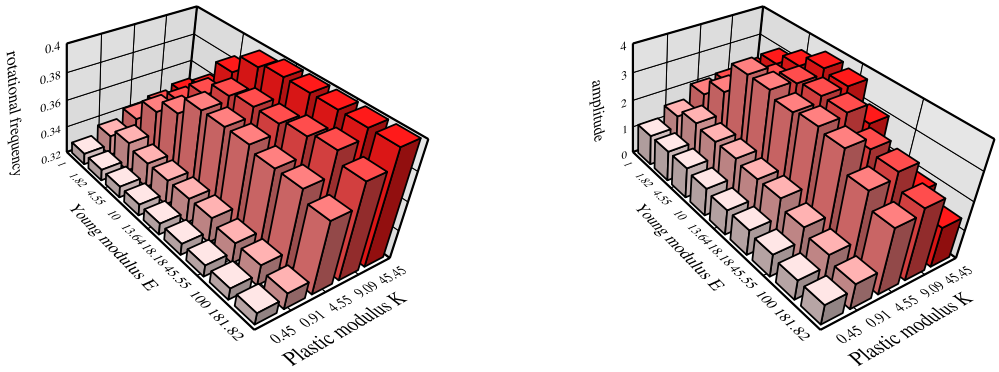

(a) $\|Y\|$ (b) Ω_c

Figure 13: Coordinates $(\|Y\|, \Omega_c)$ versus E and K

Young and plastic modulii in the *contact stiffening* phenomenon by shifting Ω_c to higher values. Very similar results are obtained for the other significant peaks of amplitude of vibration but are not detailed here for the sake of brevity.

Moreover, results are obtained after twenty rounds only. More dramatic tendencies may be detected over a longer lapsetime eventually leading to the failure of the blade. These important results confer on the abradable coating technology potential destructive side-effects in specific configurations.

7.2.2 Imperfections of the casing

Even though the dominant 2-nodal diameter shape of the casing is a preferred configuration, sensitivity to possible more complicated shapes may also be explored. Accordingly, the casing is now distorted along a combination of 2- and a 5-nodal diameter shape as depicted in Fig. 6(b) and abradable parameters are $E = 10$ and $K = 4.55$.

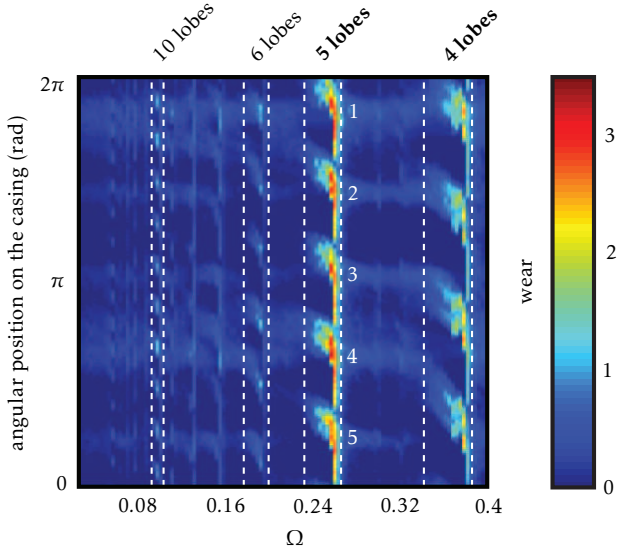

Figure 14: Abradable coating wear patterns

The shape of the casing induces five privileged and non-evenly distributed contact areas on the casing. Accordingly, five unequal worn lobes on the abradable coating are

observed in general non-critical configurations as depicted in Fig. 14. However, as compared to maps in Figs. 11, a pattern involving five lobes is predicted for $\Omega = 0.26$. The previous 4- and 6-lobe profiles are still present but not dominant. This short parameter analysis illustrates the possible co-existence of worn patterns separately exhibiting odd and even numbers of lobes. It also shows a phase-shift of the starting angular position of the pattern from one Ω to the next one in the neighborhood of a critical velocity. This is particularly apparent for the 4-lobe profile but sill unexplained.

7.2.3 Tangential efforts

The tangential contribution of the contact force is now reflected. Post-processing shows that the average ratio between the tangential and the radial components is 0.15 which seems consistent with experimental observations [12].

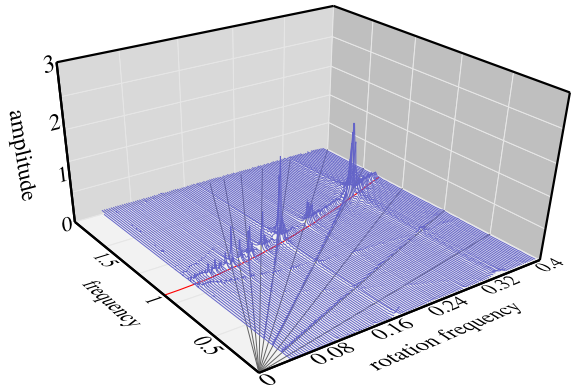

Figure 15: Blade spectrum with tangential efforts for $E = 10$ and $K = 4.55$

Comparison of Fig. 15 and Fig. 10(b) for which tangential efforts are neglected shows that the latter tend to reduce the amplitude of vibration of the blade. When the tangential component of the contact force is accounted for, high amplitudes of vibration — mostly the intersections of $f_1(\Omega)$ with $\mathrm{eo}(k)$ — occur at slightly lower rotational frequencies. This global softening in the contact case is probably due to a loosen constrained contact configuration. Moreover, the tangential efforts tend to excite the first modes of vibration of the blade in a more natural and realistic fashion.

Spectrograms of the response of the blade are given at each respective Ω_c as depicted in Fig. 16(a) when tangential contact efforts are neglected and in Fig. 16(b) when they are introduced. On each spectrogram, the predominance of the first flexural mode (mode 1) in the blade response, from the beginning to the end of the simulation, is obvious. This corresponds to the main peak of resonance indicated in Fig. 10(b). Modal participations of higher modes are also significant together with non-negligible sub and superharmonics. These components are not visible in Fig. 10(b) because of the chosen frequency range but do exist. The presence of these contributions is highly dependent on the assumed shape of the casing and the rotational velocity of the blade. Interestingly, the spectrum of the response is less disorganized when tangential forces are accounted for, which tends to corroborate the assumed more realistic vibratory solicitation of the blade. The major participations exhibit a wider frequency bandwidth in Fig. 16(a) than in Fig. 16(b) and may correspond to less physical types of response. In this line, the tangential resistance inherited from the abradable removal may be a crucial component of the model.

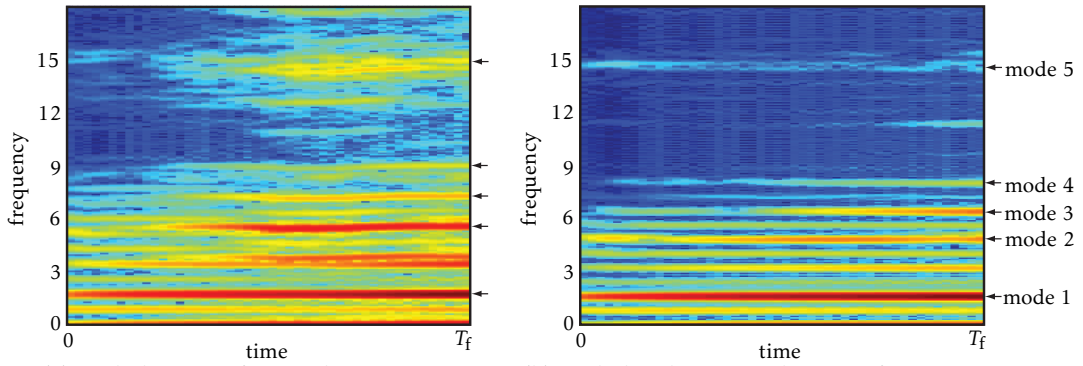

(a) Radial contact force only — $\Omega = 0.38$ (b) Radial and tangential contact forces — $\Omega = 0.35$

Figure 16: Spectrograms of the blade response

8 Conclusion

The emphasis of the study is placed on the investigation of structural contact interactions occurring between a rotating flexible blade and a surrounding rigid casing, both belonging to the low pressure compressor stage of an aircraft engine. It is now accepted that tip-rubbing will occur and tip clearances are chosen and controlled so that energy efficiency is optimum at cruise speed. They can be set tight by incorporating abradable coatings deposited on the casings, providing a rub-tolerant case surface that minimizes blade damage with attendant benefits in compressor energy efficiency. Subsequent unwanted slight rubs create grooves within the coating and deteriorate compression rates and global performances. The study focuses on a macroscopic modeling of this material removal process. The proposed numerical tool couples an explicit time-stepping procedure to a plastic constitutive law that approximates material removal. In addition, a reduced-order model of the blade of interest accounting for centrifugal stiffening effects is built.

First results exhibit complex structural behaviors with the detection of critical rotational velocities related to the eigenspectrum of the blade affected by the nonlinear terms. Results show a high sensitivity of the vibratory levels of the blade to the mechanical properties of the abradable material and a worst-case scenario is identified for which amplitudes of motion reach a maximum over twenty rounds of the blade. The slow and continuous opening of the operating clearance between the blade-tip and the casing synchronizes with the nonlinear resonance of the blade and then concedes growing vibratory amplitudes and attendant worn lobes in the liner. Accordingly, the introduced macroscopic model suggests that the abradable coatings technology may lead to unexpected higher vibrations than that originated by direct blade/casing contacts. It is also found that the tangential contribution of the contact forces slightly softens the contact conditions and yields slower but more physical unbounded blade vibratory occurrences. The versatility of the deployed tool is such that complex mechanisms like thermo- or viscoelasticity arising in abradable materials may be implemented.

9 Acknowledgement

Thanks go to Snecma for its technical and financial support. This work takes place in the framework of the MAIA mechanical research and technology program sponsored by CNRS, ONERA and SAFRAN Group.

[1] K. Andrews, M. Shillor, S. Wright, and A. Klarbring. "A dynamic thermoviscoelastic contact problem with friction and wear". *International Journal of Engineering Science* 35.14 (1997), p. 1291–1309.
DOI: 10.1016/S0020-7225(97)87426-5.

[2] N. Carpenter, R. Taylor, and M. Katona. "Lagrange constraints for transient finite element surface contact". *International Journal for Numerical Methods in Engineering* 32 (1991), p. 130 –128.
DOI: 10.1002/nme.1620320107.

[3] R.R. Craig and C.C. Bampton. "Coupling of substructures for dynamics analyses". *AIAA Journal* 6.7 (1968), p. 1313 –1319.
DOI: 10.2514/3.4741.

[4] A. Dmitriev, A. Smolin, V. Popov, and S. Psakhie. "A multilevel computer simulation of friction and wear by numerical methods of discrete mechanics and a phenomenological theory". *Physical Mesomechanics* 12.1-2 (2009), p. 11–19.
DOI: 10.1016/j.physme.2009.03.002.

[5] J. Jiang, J. Ahrens, H. Ulbrich, and E. Scheideler. "Contact model of a rotating rubbing blade". *Proceedings of the 5th International Conference on Rotor Dynamics of the IFTOMM*. Darmstadt, Germany, June 1998.

[6] T. Laursen. *Computational contact and impact mechanics - Fundamentals of modeling interfacial phenomena in nonlinear finite element analysis*. Springer-Verlag, Heidelberg, 2002. ISBN: 3540429069.

[7] D. Laxalde and M. Legrand. "Nonlinear Modal Analysis of Mechanical Systems with Frictionless Contact Interfaces". *Computational Mechanics* 47.4 (2011), p. 469–478.
DOI: 10.1007/s00466-010-0556-3.
OAI: hal.archives-ouvertes.fr:hal-00492775.

[8] M. Legrand, C. Pierre, P. Cartraud, and J.-P. Lombard. "Two-dimensional modeling of an aircraft engine structural bladed disk-casing modal interaction". *Journal of Sound and Vibration* 319.1-2 (2009), p. 366 –391.
DOI: 10.1016/j.jsv.2008.06.019.
OAI: hal.archives-ouvertes.fr:hal-00328186.

[9] N. Lesaffre, J.-J. Sinou, and F. Thouverez. "Contact analysis of a flexible bladed-rotor". *European Journal of Mechanics - A/Solids* 26.3 (2007), p. 541–557.
DOI: 10.1016/j.euromechsol.2006.11.002.

[10] X. Ma and A. Matthews. "Investigation of abradable seal coating performance using scratch testing". *Surface and Coatings Technology* 202.4-7 (2007), p. 1214–1220.
DOI: 10.1016/j.surfcoat.2007.07.076.

[11] A. Millecamps, J. F. Brunel, P. Dufrénoy, F. Garcin, and M. Nucci. "Influence of thermal effects during blade-casing contact experiments". *Proceedings of the ASME IDETC/CIE*. DETC2009-86842. San Diego, USA, Sept. 2009.

[12] C. Padova, J. Barton, M.G. Dunn, S. Manwaring, G. Young, M. Adams Jr., and M. Adams. "Development of an Experimental Capability to Produce Controlled Blade Tip/Shroud Rubs at Engine Speed". *Journal of Turbomachinery* 127.4 (2005), p. 726–735.
DOI: 10.1115/1.1934429.

[13] C. Padova, J. Barton, M. Dunn, and S. Manwaring. "Experimental Results From Controlled Blade Tip/Shroud Rubs at Engine Speed". *Journal of Turbomachinery* 129.4 (2007), p. 713–723.
DOI: 10.1115/1.2720869.

[14] E. Rabinowicz. *Friction and wear of materials*. John Wiley & Sons, Inc., New-York, 1965. ISBN: 0471830844.

[15] L. Salles, L. Blanc, F. Thouverez, and A. Gouskov. "Dynamic Analysis of Fretting Wear in Friction Contact Interfaces". *Journal of Engineering for Gas Turbines and Power* 131 (2010).
DOI: 10.1115/1.3028229.

[16] J.C. Simo and R.L. Taylor. "A return mapping algorithm for plane stress elastoplasticity". *International Journal for Numerical Methods in Engineering* 22 (1986), p. 649–670. DOI: 10.1002/nme.1620220310.

[17] J. Simo and T. Hughes. *Computational inelasticity*. Springer, 1998. ISBN: 0387975209.

[18] S.K. Sinha. "Non-linear dynamic response of a rotating radial Timoshenko beam with periodic pulse loading at the free-end". *International Journal of Non-Linear Mechanics* 40.1 (2005), p. 113–149. DOI: 10.1016/j.ijnonlinmec.2004.05.019.

[19] Arnaud Sternchüss and Etienne Balmes. "On the reduction of quasi-cyclic disk models with variable rotation speeds". *Proceedings ISMA*. France, Sept. 2006. OAI: hal.archives-ouvertes.fr:hal-00266394.

[20] N. Strömberg, L. Johansson, and A. Klarbring. "Derivation and analysis of a generalized standard model for contact, friction and wear". *International Journal of Solids and Structures* 33.13 (1996), p. 1817–1836. DOI: 10.1016/0020-7683(95)00140-9.

[21] Y.F. Wang and Z.G. Yang. "Finite element model of erosive wear on ductile and brittle materials". *Wear* 265.5-6 (2008), p. 871–878. DOI: 10.1016/j.wear.2008.01.014.

[22] R. J. Williams. "Simulation of blade casing interaction phenomena in gas turbines resulting from heavy tip rubs using an implicit time marching method". *Proceedings of the ASME Turbo Expo 2011*. GT2011-45495. Vancouver, Canada, June 2011.

[23] P. Wriggers. *Computational contact mechanics*. Wiley, 2002. ISBN: 3540326081.

[24] M. Yi, J. He, B. Huang, and H. Zhou. "Friction and wear behaviour and abradability of abradable seal coating". *Wear* 231.1 (1999), p. 47–53. DOI: 10.1016/S0043-1648(99)00093-9.